

# Origin of the complex iron line structure and spectral variation in Mrk 766

Yuto Mochizuki<sup>1,2</sup>  <sup>★</sup>, Misaki Mizumoto<sup>3</sup> , and Ken Ebisawa<sup>1,2</sup> 

<sup>1</sup>*Institute of Space and Astronautical Science (ISAS), Japan Aerospace Exploration Agency (JAXA), 3-1-1 Yoshinodai, Chuo-ku, Sagamihara, Kanagawa 252-5210, Japan*

<sup>2</sup>*Department of Astronomy, Graduate School of Science, The University of Tokyo, 7-3-1 Hongo, Bunkyo-ku, Tokyo 113-0033, Japan*

<sup>3</sup>*Science education research unit, University of Teacher Education Fukuoka, 1-1 Akama-bunkyo-machi, Munakata, Fukuoka 811-4192, Japan*

Accepted 2023 July 27. Received 2023 July 10; in original form 2023 April 3

## ABSTRACT

Complex Fe-K emission/absorption line features are commonly observed in the 6–11 keV band from Active Galactic Nuclei (AGN). These features are formed in various physical components surrounding the black holes. The Narrow-Line Seyfert 1 (NLS1) galaxy Mrk 766, in particular, exhibits characteristic blue-shifted Fe-K absorption lines caused by the ultra-fast outflow (UFO), and a broad Fe-K emission line, as well as variable absorbers partially covering the X-ray emitting region. We re-analyze the Mrk 766 archival data of *XMM-Newton*, *NuSTAR*, and *Swift* to investigate the origin of the Fe-K line feature and the 0.3–79 keV energy spectral variation. We have found that the spectral variation in  $\leq 10$  keV is primarily explained by the variable partial covering of the central X-ray source by multi-layer absorbing clouds. The Fe-K line feature consists of the blue-shifted absorption lines due to the UFO, a narrow emission line from the distant material, a broad emission line from the inner-disk reflection, and a slightly broadened weak emission line at around 6.4–6.7 keV whose equivalent width is  $\sim 0.05$  keV. The last one is presumably due to the resonance scattering in the UFO out of the line-of-sight, as predicted by a Monte Carlo simulation based on the hydrodynamical UFO modeling. We suggest that the seemingly complex Fe-K line features and the X-ray energy spectra of Mrk 766 are explained by a moderately extended central X-ray source around a Schwarzschild black hole, an optically thick accretion disk with a truncated inner-radius, the UFO, multi-layer partial covering clouds, and a torus.

**Key words:** galaxies: active – galaxies: Seyfert – X-rays: individual: Mrk 766

## 1 INTRODUCTION

X-ray radiation from Active Galactic Nuclei (AGN) is reprocessed by surrounding materials around the central black hole, such as the accretion disk, torus, outflow, and various ionized gases, which affect the X-ray energy spectrum. Absorption lines are produced by the intervening hot plasma, while the emission lines result from fluorescence or recombination in the surrounding materials. In particular, complex Fe-K spectral features, often observed in the 6–9 keV band, arise due to multiple absorbers and scatterers around the black holes. By resolving the complex Fe-K line structure, we can gain a deeper understanding of the physical properties and processes in the vicinity of the black hole.

Mrk 766 is classified as a Narrow-line Seyfert 1 (NLS1) galaxy with a black hole mass of  $\log(M_{\text{BH}}/M_{\odot}) = 6.82^{+0.05}_{-0.06}$  (Bentz & Katz 2015) at a cosmic redshift of  $0.01271 \pm 0.00005$  (Adelman-McCarthy et al. 2011). Over the past few decades, this source has been extensively observed with *XMM-Newton*, *NuSTAR*, and *Swift*.

Mrk 766 has the following two notable X-ray characteristics: First, significant X-ray flux/spectral variability with a timescale of less than a day has been observed, such that the soft ( $\leq 5$  keV) X-ray band appears to be more variable than the hard band (e.g., Risaliti et al. 2011a). This spectral variation is commonly explained by the partial covering of the central X-ray source by clumpy absorbers (e.g.,

Risaliti et al. 2009a; Risaliti et al. 2009b). Various models have been proposed to describe the geometry of these clouds; double ionized layers (Miller et al. 2007; Turner et al. 2007), cometary shape with ionized and neutral layers (Risaliti et al. 2011a, Maiolino et al. 2010), a single ionized (Liebmann et al. 2014) or neutral layer (Buisson et al. 2018).

Second, the X-ray spectra show characteristic Fe-K emission and absorption structures in 6–11 keV. A hint of the ionized Fe absorption lines has been reported (Pounds et al. 2003a), and recent studies indicate presence of the blueshifted ionized Fe-K absorption lines caused by the outflowing ionized absorbers in the line-of-sight (e.g., Miller et al. 2007; Turner et al. 2007; Risaliti et al. 2011a; Liebmann et al. 2014; Buisson et al. 2018). The outflow velocity,  $\sim 0.1c$ , is categorized as an ultra-fast outflow (UFO; Pounds et al. 2003a,b; Reeves et al. 2009). The ionization parameter of these absorbing clouds is  $\xi \sim 10^{3-5}$  erg cm s<sup>-1</sup> and the hydrogen column density is  $N_{\text{H}} \sim 10^{22-24}$  cm<sup>-2</sup> (e.g., Tombesi et al. 2011). In addition, a broad Fe-K emission line is observed in 6–7 keV. Liebmann et al. (2014) and Buisson et al. (2018) explained this broad line assuming the disk reflection caused by a tiny corona in the very vicinity of the fast-rotating black hole, subject to the strong relativistic distortion (e.g., Fabian et al. 2009).

Both the partial covering and the Fe-band spectral features have to be reconciled in the X-ray spectral modeling of Mrk 766. However, the relationship between the partial covering clouds, UFOs, and the broad Fe emission lines remains unclear. In particular, the relativistic

\* E-mail: mochizuki@ac.jaxa.jp

line-broadening requires the tiny X-ray emission region located in the close vicinity of the black hole. Such a very compact X-ray source should not be *partially* but *fully* covered by the absorbing clouds in the line-of-sight (e.g., [Iso et al. 2016](#)). Thus, it is required to scrutinize the origin of the partial covering clouds, UFOs, and the broad Fe emission lines to build a consistent picture of the X-ray emission mechanism in Mrk 766 and other similar Seyfert galaxies.

This paper aims to reveal the origin of the complex Fe-K line structure in Mrk 766, and to propose a consistent X-ray spectral model based on the realistic AGN spectral components. Section 2 describes the method of data analysis, Section 3 presents our spectral fitting models and the fitting results. The results are discussed in Section 4 and the paper is concluded in Section 5.

## 2 OBSERVATION AND DATA REDUCTION

We used the archival data of *XMM-Newton*, *NuSTAR*, and *Swift*. The datasets are listed in Table 1.

All the available *XMM-Newton* ([Jansen et al. 2001](#)) archival data to date were used. In the data analysis, the Science Analysis Software (SAS, v.19.1.0) ([Gabriel et al. 2004](#)) and the calibration files corresponding to this SAS version were used. In the European Photon Imaging Camera (EPIC)-pn ([Strüder et al. 2001](#)), `epchain` was used to produce the clean events. From each observation ID, a single spectrum was produced; in total, we made nine spectral datasets. The source spectra were extracted from a circular region of a radius of  $30''$  centered on the source with `PATTERN<=4`. The background spectra were extracted from a circular region of a radius of  $45''$  in the same CCD chip near the source, avoiding the chip edges and/or the serendipitous sources, and minimizing the effects of the Cu-K background lines. High background periods were excluded when the count rates in 10–12 keV with `PATTERN==0` were higher than  $0.4 \text{ cts s}^{-1}$ . By using `epatplot`, a possible pile-up effect in the source region was examined. The only full-window mode data, XMM9, was affected by the pile-up and hollowed at the center with a circle of  $10''$  radius. Other observations were performed in the small-window mode and were not affected by the pile-up. In addition, we made a merged spectrum by combining all the XMM-pn spectra with `epicombine`. In the Reflection Grating Spectrometer (RGS) ([den Herder et al. 2001](#)), `rgsproc` was used to create the cleaned events with the same good time intervals of XMM-pn. The RGS1 and the RGS2 spectra of each observation ID were combined using `rgscombine`.

We also used all the available *NuSTAR* ([Harrison et al. 2013](#)) archival data. The *NuSTAR* data analysis software (v.2.1.2) in HEASOFT (v.6.30.1) with the contemporary calibration files (20220926) were used. `nupipeline` was run to create the clean events for both the focal plane modules (FPMA and FPMB). The source spectra were extracted from a circular region of  $40''$  radius centered on the source by using `nuproduct`. The background spectra were extracted from a circular region of  $150''$  radius near the source region.

We also used the *Swift* ([Gehrels et al. 2004](#)) archival data which was taken simultaneously with *NuSTAR* (Nu10). The *Swift* XRT data was reduced using HEASOFT (v.6.30.1) to produce the clean events. The source spectrum was extracted from a circular region of a radius of  $40''$  centered on the source. The background spectrum was extracted from a circular region of a radius of  $150''$  from the nearby blank region.

The XMM-pn, *NuSTAR* and *Swift* spectra were rebinned to enhance the visibility around the UFO feature depending on the counting rates and exposure time; at least 400 counts per new energy-bin

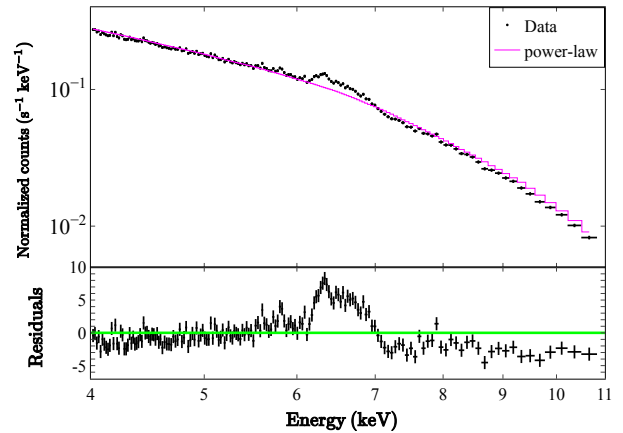


**Figure 1.** Spectral fitting result of the merged XMM-pn spectrum with a power-law. The spectrum was re-binned to have 1,500 counts per new spectral bin. In the top panel, the merged XMM-pn spectrum is shown in black and power-law function in magenta. The bottom panel shows the residuals in the unit of standard deviation.

for XMM2 and Nu10, 50 counts for XMM9 and Nu11 and Sw12, and 200 counts for the other spectra. All the XMM-RGS spectra were binned to have at least 25 counts per new energy-bin.

In the following, we tried to construct a model which explains the XMM-pn and XMM-RGS spectra simultaneously, as well as the *NuSTAR* and *Swift* spectra when available. The energy ranges we used for XMM-pn, XMM-RGS, *NuSTAR*, *Swift* are 0.3–11 keV, 0.33–2 keV, and 3–79 keV, 0.3–7.5 keV, respectively. All the spectral fittings were performed by using `xspec` v.12.12.1 ([Arnaud 1996](#)), where we employed the  $\chi^2$ -statistics. The error values correspond to the 90 % confidence level.

## 3 RESULTS

### 3.1 Complex Fe-K line structure

First, we demonstrate the complex Fe line structure in Mrk 766. We analyzed the merged spectrum of all the XMM-pn data in 4–11 keV by fitting with a power-law (Fig. 1). We can clearly see the complex Fe-K structure, a narrow emission line at 6.4 keV, a broad emission feature in 6–7 keV, and blue-shifted absorption lines in 7–11 keV. Also, we can recognize a weak emission line at  $\sim 5.8$  keV which is presumably the Mn-K line. Below, we are going to explain these spectral features as well as the continuum spectral components.

### 3.2 A double-layer partial covering model

We adopted a double-layer partial covering model, which is known to explain the broadband X-ray spectral variability (e.g., [Risaliti et al. 2011a](#)). Since the change in the column density of an optically-thin partial absorber is mathematically indistinguishable from the change in the partial covering fraction (e.g., [Miyakawa et al. 2012](#); [Mizumoto et al. 2014](#)), the two partial covering fractions can be the same by adjusting the column densities. This model is called the variable double partial covering (VDPC) model ([Mizumoto et al. 2014](#)), and has been successful to explain spectral variations of a dozen of Seyfert galaxies ([Miyakawa et al. 2012](#); [Iso et al. 2016](#); [Yamasaki et al. 2016](#); [Midooka et al. 2022](#)). Hereafter the partial covering fraction is denoted as  $\alpha$ , where  $0 \leq \alpha \leq 1$ .

**Table 1.** List of the archive data used in this paper

Name	ID	Date	Exposure (s)* <sup>1</sup>	Count rate (s <sup>-1</sup> )* <sup>2</sup>
XMM1	0096020101	2000.05.20	25,544	13.3
XMM2	0109141301	2001.05.20	88,243	22.6
XMM3	0304030101	2005.05.23	65,193	3.9
XMM4	0304030301	2005.05.25	68,938	8.6
XMM5	0304030401	2005.05.27	65,767	11.3
XMM6	0304030501	2005.05.29	64,526	14.0
XMM7	0304030601	2005.05.31	60,698	11.7
XMM8	0304030701	2005.06.03	20,089	10.0
XMM9* <sup>3</sup>	0763790401	2015.07.05	19,534	4.7
Nu10	60001048002	2015.01.24	90,107	0.4
Nu11	60101022002	2015.07.05	23,545	0.3
Sw12	00080076002	2015.01.25	4,885	1.0

\*<sup>1</sup> After removing the background flare periods.

\*<sup>2</sup> In 0.3–11 keV for XMM-pn data, and in 3–79 keV for *NuSTAR* data (averaging FPAM and FPMB).

\*<sup>3</sup> Full-window mode.

The model we used is expressed as follows:

$$\begin{aligned}
 F = & \{(1 - \alpha + \alpha * W_1)(1 - \alpha + \alpha * W_2) \\
 & (\text{powerlaw} + \text{const}_{\text{ref}} * \text{relxill} + \text{diskbb}) * W_3 * W_4 \\
 & + \text{pexmon} + \text{const}_{\text{Mn}} * G_{\text{Mn}}\} \\
 & * \text{const}_{\text{cross}} * \text{zTBabs} * \text{TBabs}.
 \end{aligned} \quad (1)$$

In the following, we explain the individual spectral components:

(1) **powerlaw**: The intrinsic X-ray component from the central X-ray source is modeled with a power-law function in the concerned energy range (0.3 – 79 keV).

(2) **const<sub>ref</sub>\*relxill**: The inner disk reflection is modeled using **relxill v.2.1** (García et al. 2014; Dauser et al. 2014, 2022). The black hole spin parameter  $a$  is fixed at 0 and the emissivity index is set to 3, which are the nominal values for the Schwarzschild black hole. The inner and outer disk radius are  $6 R_g$  and  $400 R_g$ , respectively, where  $R_g$  is the gravitational radius. The **relxill** normalization is made equal to the **powerlaw** one. The reflection rate relative to the direct X-ray emission (**const<sub>ref</sub>**) and the ionization parameter of the disk are free parameters common to all the spectra. The inclination angle with respect to the line-of-sight is assumed to be 60 deg, since Mrk 766 is classified as a “complex” NLS1 which tends to have a high inclination angle (Gardner & Done 2015). The cut-off energy, Fe abundance, and redshift of **relxill** are fixed at 1,000 keV, the solar abundance, and the cosmic redshift, respectively (Table 2).

(3) **pexmon**: A narrow emission line at 6.4 keV corresponding to the fluorescent Fe-K line was observed within all the spectra. Therefore we introduced **pexmon**, which represents the reflection by a distant neutral disk or torus (Magdziarz & Zdziarski 1995; Nandra et al. 2007). The photon index and normalization are set equal to those of **powerlaw** component, and the inclination, abundance, cut-off energy, and redshift are fixed at those of the **relxill** model. The only free parameter in this model is the reflection rate, which is tied across all the spectra. The reflection rate corresponds to  $\Omega/2\pi$ , where  $\Omega$  is the solid angle of the reflector.

(4) **diskbb**: To explain the soft excess component, we adopted the phenomenological disk blackbody model, **diskbb** (Mitsuda et al. 1984; Makishima et al. 1986). The normalization is dimensionless value given by  $(R_{\text{in}}/D_{10})^2 \cos \theta$ , where  $R_{\text{in}}$  is the inner disk radius in km,  $D_{10}$  is the distance to the X-ray source in 10 kpc, and  $\theta$  is the inclination angle of the disk. The normalization is allowed to vary

independently for each spectrum. The inner disk temperature ( $T_{\text{in}}$ ) is tied across all the spectra.

(5) **TBabs** and **zTBabs**: The Galactic H I column density toward Mrk 766 is  $1.85 \times 10^{20} \text{ cm}^{-2}$  (LAB map; Kalberla et al. 2005), which is modelled by **TBabs** (Verner et al. 1996; Wilms et al. 2000). The host galaxy absorption is modeled by **zTBabs**, whose column density is a free parameter and the cosmic redshift is fixed.

(6)  $W_i$ , where  $i$  is from 1 to 4: Photo-ionized absorbers calculated with **MPI\_XSTAR** (Danehkar et al. 2018), which is an implementation of the photo-ionized simulation code **xstar** (v.2.58e; Kallman et al. 2004) incorporating the Message Passing Interface (MPI). The table models are calculated assuming a power-law incident spectrum ( $\Gamma = 2.2$ ) and discrete values of the column density, ionization parameter, and turbulent velocity. Table 3 shows the parameter grids adopted.

$W_1$  and  $W_2$  are for the double-layer partial covering clouds, and  $W_3$  represents the full-covering ionized warm absorber (Tombesi et al. 2013). For these three absorbers, we use the same table model, where the line-of-sight velocity in the rest-frame and the turbulent velocity are fixed to null. The ionization parameter was calculated between  $10^{-2}$  and  $10^5$  with 20 logarithmically spaced intervals, and the column density was calculated between  $0.01 \times 10^{22} \text{ cm}^{-2}$  and  $1000 \times 10^{22} \text{ cm}^{-2}$  with 20 logarithmically spaced intervals (400 grid points in total). Column densities and ionization parameters of each of the three absorbers are assumed to be invariable throughout the observational period. In the double-layer absorber,  $W_1$  represents the higher-ionized layer while  $W_2$  is for the lower-ionized core. The covering fraction  $\alpha$  is a free parameter for each spectrum. The partial covering clouds are assumed to intervene the central X-ray emitting components, namely, **powerlaw** + **const<sub>ref</sub>\*relxill** + **diskbb** in Eq. (1), but not **pexmon** that is considered to be located further from the black hole than the partial covering clouds.

$W_4$  represents the UFO, where both the line-of-sight velocity and the turbulent velocity are free parameters. The ionization parameter was calculated between  $10^3$  and  $10^5$  with 20 logarithmically spaced intervals, and the column density was calculated between  $0.01 \times 10^{22} \text{ cm}^{-2}$  and  $100 \times 10^{22} \text{ cm}^{-2}$  with 20 logarithmically spaced intervals. In addition, the turbulent velocity was calculated between  $100 \text{ km s}^{-1}$  and  $10,000 \text{ km s}^{-1}$  with 5 logarithmically spaced inter-

**Table 2.** Fixed parameter in our spectral model.

model	parameter	value
TBabs	$N_{\text{H}} (10^{20} \text{cm}^{-2})$	1.85
relxill	Emissivity index	3
	Spin parameter( $a$ )	0
	Inclination (degree)	60
	$r_{\text{in}} (R_{\text{g}})$	6
	$r_{\text{out}} (R_{\text{g}})$	400
	Abundance	Solar abundance* <sup>1</sup>
	Cut-off-Energy (keV)	1000

\*<sup>1</sup> Grevesse & Sauval (1998)**Table 3.** Parameter grids of the table models calculated by MPL\_XSTAR

parameter	$W_1 - W_3$	$W_4$
$N_{\text{H}} (10^{22} \text{cm}^{-2})$	0.01 - 1000	0.01 - 100
$\log \xi$	-2 - 5	3 - 5
vturb (km s <sup>-1</sup> )* <sup>1</sup>	0 (fixed)	100 - 10,000
number of grids* <sup>2</sup>	400	2,000

\*<sup>1</sup> Turbulent velocity in the absorbing plasma.\*<sup>2</sup>  $N_{\text{H}}$ ,  $\xi$  and vturb are logarithmically equally delimited by 20, 20, and 5, respectively

vals (2,000 grid points in total). All the  $W_4$  parameters are allowed to be free for each spectrum.

(7) `constcross` gives a cross-calibration adjustment between XMM-pn and *NuSTAR* or between *Swift* and *NuSTAR*.

(8) `constMn * GMn`: The Mn-K $\alpha$  line feature (§3.1) is modeled by a positive Gaussian. Normalization of the line is assumed to be proportional to that of `powerlaw`. The ratio, `constMn`, is tied for all the spectra.

### 3.3 Spectral fitting

We conducted simultaneous spectral fitting using the model in Eq. (1) for all the 10 spectral datasets; XMM1–8, XMM9 & Nu11, and Nu10 & Sw12. We try to find a solution that the disk geometry and properties of the partial and warm absorbers exhibit minimal variations over the entire observation for ~15 years. Accordingly, we have fixed several parameters at constant values (Table 2), tied some other parameters for all the ten datasets (Table 4), and allowed the remainder to vary for each dataset (Table 5).

Fig. 2 (left) shows fitting result of XMM2 (the brightest one) and XMM3 (the dimmest one) in 0.3 – 11 keV with the double partial covering model in Eq. (1). We found significant residuals at ~0.55 keV and 6.4–6.7 keV. The former is likely to be the O VII line from the photoionized plasma (Buisson et al. 2018), for which we introduce a Gaussian line ( $G_{\text{OVII}}$ ) for further analysis with its normalization and energy being tied for the 10 datasets. Fig. 2 (center) shows expansion of the left-panels in 4 – 10 keV to demonstrate the residual at 6.4–6.7 keV, which is more prominent in the brighter spectrum. To explain this feature, we add a Gaussian line ( $G_{\text{Fe}}$ ) (Fig. 2 right), whose origin will be discussed in §4.4. The normalization, energy, and intrinsic width of  $G_{\text{Fe}}$  are made free parameters for each dataset. We also remark that the UFO absorption feature and the partial covering feature (manifested by the spectral flattening below

**Table 4.** Fitting results of the tied parameters in the double-layer partial covering model

model	parameter	value
zTBabs	$N_{\text{H}} (10^{20} \text{cm}^{-2})$	$1.53^{+0.02}_{-0.02}$
$W_1$	$N_{\text{H}} (10^{23} \text{cm}^{-2})$	$3.89^{+0.08}_{-0.08}$
	$\log \xi$	$1.68^{+0.01}_{-0.02}$
$W_2$	$N_{\text{H}} (10^{22} \text{cm}^{-2})$	$2.10^{+0.03}_{-0.03}$
	$\log \xi$	< -2
$W_3$	$N_{\text{H}} (10^{21} \text{cm}^{-2})$	$2.87^{+0.01}_{-0.01}$
	$\log \xi$	$0.478^{+0.004}_{-0.004}$
diskbb	$T_{\text{in}}$ (keV)	$0.1316^{+0.0001}_{-0.0001}$
powerlaw	$\Gamma$	$2.24^{+0.02}_{-0.01}$
relxill	$\log \xi$	$0.30^{+0.01}_{-0.03}$
const <sub>ref</sub>	powerlaw ratio	$0.0090^{+0.0003}_{-0.0004}$
pexmon	Reflection rate	$-0.26^{+0.02}_{-0.02}$
$G_{\text{OVII}}$	Energy (keV)	$0.5543^{+0.0000}_{-0.0002}$
	$\sigma$ (keV)	$0.001^{+0.001}_{-0.000}$
	normalization ( $10^{-5}$ photons s <sup>-1</sup> cm <sup>-2</sup> )	$2.4^{+0.3}_{-0.7}$
$G_{\text{Mn}}$	Energy (keV)	$5.76^{+0.05}_{-0.07}$
	$\sigma$ (keV)	$0.09^{*1}$
const <sub>Mn</sub>	powerlaw ratio	$0.0002^{+0.0001}_{-0.0001}$

\*<sup>1</sup> not constrained

~6 keV) are more prominent in the dimmer spectrum, as suggested by Turner et al. (2007) and Risaliti et al. (2011a). The simultaneous fitting results of the 10 datasets in 0.3 – 79 keV are shown in Fig. 3 and Tables 4 and 5.

### 3.4 The triple partial covering model

As shown in Fig. 3 and Table 5, the double partial covering model can explain all the 10 spectral datasets taken over ~15 years with most significantly variable parameters being the power-law normalization and the partial covering fraction. The left panel of Fig. 4 displays the power-law normalization versus the covering fraction for the 10 datasets, which indicates a negative correlation between the two parameters. This negative correlation is unexpected, since the intrinsic X-ray luminosity, which is supposed to be proportional to the power-law normalization, and the geometrical covering fraction of the X-ray emitting region by the outer clumps should not be directly connected.

First, we examine whether the electron scattering of X-rays out of the line of sight due to the partial covering clouds could explain this correlation. We add the `cabs` model for the electron scattering to the partial absorber, where the column density is fixed to the sum of the two partial covering clouds. Even in this case, the negative correlation does not disappear (the center panel of Fig. 4).

Next, we propose the presence of the third partial covering layer which is completely opaque (e.g., Miyakawa et al. 2012). In this case, as the partial covering fraction increases, the intrinsic X-rays are more blocked, and the power-law normalization decreases apparently, even if the intrinsic X-ray luminosity does not vary. Thus, we adopt the "triple partial covering model", which extends the double-layer partial covering model by including an additional neutral core ( $W_5$ ).

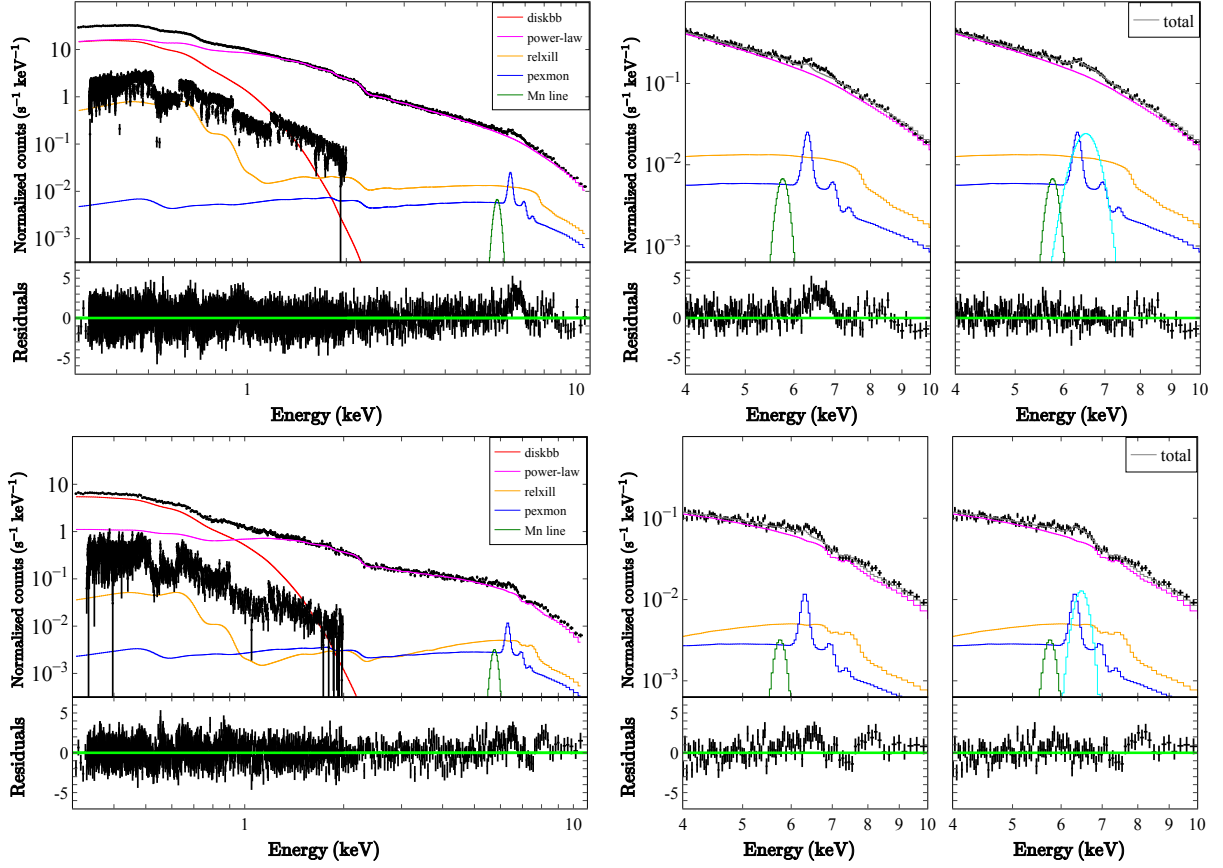


**Figure 2.** (left panels) Spectra fitting results of XMM2 (upper) and XMM3 (lower) in 0.3–11 keV with the model shown in Eq. (1). The black shows the observed spectra and residuals for EPIC-pn and RGS, and the red, magenta, orange, blue, green, and gray lines show the best-fit EPIC-pn components of *diskbb*, *powerlaw*, *relxill*, *pexmon*,  $G_{\text{Mn}}$ , and the total model spectrum, respectively. (center panels) Expansion of the left-panels in 4 – 10 keV. (right panels) Fitting with an additional iron emission line  $G_{\text{Fe}}$  (cyan).

The third partial covering layer is modeled using *zpcfabs* with the abundance by Wilms et al. (2000). We can express the triple partial covering model as

$$\begin{aligned}
 F = & \{(1 - \alpha + \alpha * W_5)(1 - \alpha + \alpha * W_1)(1 - \alpha + \alpha * W_2) \\
 & (\text{powerlaw} + \text{const}_{\text{ref}} * \text{relxill} + \text{diskbb}) * W_3 * W_4 \\
 & + \text{pexmon} + \text{const}_{\text{Mn}} * G_{\text{Mn}} + G_{\text{Fe}} + G_{\text{OVII}}\} \\
 & * \text{const}_{\text{cross}} * z\text{TBabs} * \text{TBabs}.
 \end{aligned} \quad (2)$$

We can explain all the data with the triple partial covering model (Fig. 5, Tables 6 and 7) as well as with the double partial covering model. The right panel of Fig. 4 shows the relation between the power-law normalization and the covering fraction in the triple partial covering model, which does not show the obvious correlation. Therefore, we consider that the triple partial covering model is more preferable to the double-layer partial covering model.

## 4 DISCUSSION

### 4.1 Geometry of the disc and torus

In the spectral analysis, we introduced an outer disk/torus reflection represented by the *pexmon* model, where the solid angle of the outer disk or torus was  $\Omega/2\pi = 0.20 \pm 0.01$  (with the triple partial covering model). On one hand, if there is an isotropic radiation source on nearly infinite size of the reflector, the solid angle of the reflector will be

as large as  $\Omega/2\pi \approx 1$ . On the other hand, solid angle of the upper-half of the outer torus with a half-opening angle  $\theta$ , seen from the central illuminating source, is estimated as  $\Omega/2\pi \approx \cos \theta$ . Therefore, the half-opening angle of the torus is estimated to be  $78 \pm 1$  deg, equivalent to the torus angular width  $90 - (78 \pm 3) = 12 \pm 1$  deg. Recently, it has been pointed out that Seyfert galaxies commonly have X-ray clumpy torii with small angular widths, such as  $\sim 15$  deg in the Circinus galaxy (Tanimoto et al. 2019),  $\sim 10$  deg in IC 4329A (Ogawa et al. 2019), and  $\sim 20$  deg in NGC 7469 (Ogawa et al. 2019). The small solid angle of the cold reflector we found in Mrk 766 is consistent with the reflection from such an outer clumpy torus with relatively small angular width.

Also, we estimate the inner disk reflection rate of the *relxill* model. We compare  $\text{const}_{\text{ref}} * \text{relxill}$  and  $\text{rdblur} * \text{pexrav}$  (Fabian et al. 1989; Magdziarz & Zdziarski 1995), because the latter gives a more intuitive interpretation of the normalization. In this manner, we estimate the inner disk reflection rate to be  $\Omega/2\pi \sim 0.3$ . We assume that the X-ray radiating corona is isotropic and slightly extended, so that it is *partially* covered by smaller clumps in the outer parts. It is difficult to estimate the corona size, but let's assume a radius of  $\sim 10 R_g$ . The solid angle of the inner reflecting disk, seen from a point above the black hole, is estimated as  $\Omega/2\pi \approx \cos \phi - \cos \psi$ , where  $\phi$  is the angle between the black hole and the innermost radius, and  $\psi$  is the one between the black hole and the outermost radius. If seen from the height of  $10 R_g$  above the black hole, the inner disk reflection with  $r_{\text{in}} = 6 R_g$  and  $r_{\text{out}} = 400 R_g$  gives the solid angle as

**Table 5.** Fitting results of the free parameters with the double-layer partial covering model

model	parameter	XMM1	XMM2	XMM3	XMM4	XMM5
W <sub>1</sub> &W <sub>2</sub>	$\alpha$	0.186 <sup>+0.005</sup> <sub>-0.001</sub>	< 0.000	0.643 <sup>+0.001</sup> <sub>-0.001</sub>	0.270 <sup>+0.001</sup> <sub>-0.001</sub>	0.195 <sup>+0.001</sup> <sub>-0.001</sub>
W <sub>4</sub>	$N_{\text{H}} (10^{23} \text{cm}^{-2})$	0.8 <sup>+0.2</sup> <sub>-0.2</sub>	< 1.8	0.89 <sup>+0.34</sup> <sub>-0.30</sub>	0.61 <sup>+0.16</sup> <sub>-0.15</sub>	2.06 <sup>+0.97</sup> <sub>-0.69</sub>
	$\log \xi$	3.73 <sup>+0.06</sup> <sub>-0.04</sub>	> 4.2	3.89 <sup>+0.15</sup> <sub>-0.11</sub>	3.86 <sup>+0.09</sup> <sub>-0.06</sub>	4.11 <sup>+0.16</sup> <sub>-0.10</sub>
	vturb ( $10^3 \text{km s}^{-1}$ )	1.4 <sup>+1.4</sup> <sub>-0.7</sub>	0.3 <sup>*1</sup>	0.6 <sup>+2.1</sup> <sub>-0.5</sub>	> 7.0	< 0.1
	z	-0.100 <sup>+0.002</sup> <sub>-0.002</sub>	-0.271(fixed)	-0.038 <sup>+0.003</sup> <sub>-0.008</sub>	-0.065 <sup>+0.003</sup> <sub>-0.003</sub>	-0.066 <sup>+0.003</sup> <sub>-0.001</sub>
diskbb	normalization ( $10^3$ )	7.81 <sup>+0.06</sup> <sub>-0.06</sub>	7.89 <sup>+0.03</sup> <sub>-0.03</sub>	13.6 <sup>+1.3</sup> <sub>-1.0</sub>	5.90 <sup>+0.03</sup> <sub>-0.03</sub>	5.88 <sup>+0.03</sup> <sub>-0.03</sub>
powerlaw	normalization ( $10^{-2}$ photons $\text{s}^{-1} \text{cm}^{-2} \text{keV}^{-1}$ )	0.907 <sup>+0.003</sup> <sub>-0.003</sub>	1.156 <sup>+0.002</sup> <sub>-0.002</sub>	0.560 <sup>+0.003</sup> <sub>-0.003</sub>	0.705 <sup>+0.002</sup> <sub>-0.002</sub>	0.815 <sup>+0.002</sup> <sub>-0.002</sub>
G <sub>Fe</sub>	Energy (keV)	6.61 <sup>+0.14</sup> <sub>-0.15</sub>	6.53 <sup>+0.05</sup> <sub>-0.05</sub>	6.48 <sup>+0.06</sup> <sub>-0.07</sub>	6.40 <sup>+0.07</sup> <sub>-0.07</sub>	6.68 <sup>+0.10</sup> <sub>-0.10</sub>
	$\sigma$ (keV)	0.17 <sup>+0.15</sup> <sub>-0.09</sub>	0.28 <sup>+0.05</sup> <sub>-0.05</sub>	0.16 <sup>+0.12</sup> <sub>-0.04</sub>	0.13 <sup>+0.07</sup> <sub>-0.05</sub>	0.17 <sup>+0.10</sup> <sub>-0.07</sub>
	normalization ( $10^{-5}$ photons $\text{s}^{-1} \text{cm}^{-2}$ )	0.79 <sup>+0.43</sup> <sub>-0.42</sub>	2.61 <sup>+0.35</sup> <sub>-0.34</sub>	0.84 <sup>+0.21</sup> <sub>-0.20</sub>	0.68 <sup>+0.21</sup> <sub>-0.21</sub>	0.69 <sup>+0.25</sup> <sub>-0.25</sub>
$\chi^2/\text{d.o.f}$		1.13	1.32	1.34	1.13	1.18
model	parameter	XMM6	XMM7	XMM8	XMM9&Nu11	Nu10&Sw12
W <sub>1</sub> &W <sub>2</sub>	$\alpha$	0.186 <sup>+0.004</sup> <sub>-0.001</sub>	0.180 <sup>+0.001</sup> <sub>-0.001</sub>	0.226 <sup>+0.002</sup> <sub>-0.002</sub>	0.128 <sup>+0.018</sup> <sub>-0.019</sub>	0.088 <sup>+0.010</sup> <sub>-0.010</sub>
W <sub>4</sub>	$N_{\text{H}} (10^{23} \text{cm}^{-2})$	1.05 <sup>+0.37</sup> <sub>-0.26</sub>	0.93 <sup>+0.32</sup> <sub>-0.29</sub>	0.51 <sup>+0.19</sup> <sub>-0.19</sub>	> 5.3	7.6 <sup>+2.1</sup> <sub>-1.8</sub>
	$\log \xi$	4.27 <sup>+0.13</sup> <sub>-0.12</sub>	4.08 <sup>+0.13</sup> <sub>-0.09</sub>	3.77 <sup>+0.13</sup> <sub>-0.08</sub>	4.66 <sup>+0.26</sup> <sub>-0.19</sub>	4.46 <sup>+0.14</sup> <sub>-0.56</sub>
	vturb ( $10^3 \text{km s}^{-1}$ )	3.2 <sup>+4.3</sup> <sub>-1.4</sub>	3.8 <sup>+5.0</sup> <sub>-2.5</sub>	> 0.69	< 0.8	< 0.28
	z	-0.074 <sup>+0.005</sup> <sub>-0.008</sub>	-0.052 <sup>+0.002</sup> <sub>-0.002</sub>	-0.072 <sup>+0.009</sup> <sub>-0.011</sub>	-0.145 <sup>+0.002</sup> <sub>-0.002</sub>	-0.080 <sup>+0.010</sup> <sub>-0.014</sub>
diskbb	normalization ( $10^3$ )	6.97 <sup>+0.04</sup> <sub>-0.04</sub>	5.58 <sup>+0.09</sup> <sub>-0.04</sub>	5.2 <sup>+0.06</sup> <sub>-0.06</sub>	4.50 <sup>+0.09</sup> <sub>-0.08</sub>	< 0.24
powerlaw	normalization ( $10^{-2}$ photons $\text{s}^{-1} \text{cm}^{-2} \text{keV}^{-1}$ )	1.015 <sup>+0.002</sup> <sub>-0.002</sub>	0.857 <sup>+0.002</sup> <sub>-0.002</sub>	0.794 <sup>+0.004</sup> <sub>-0.004</sub>	0.914 <sup>+0.005</sup> <sub>-0.005</sub>	1.094 <sup>+0.031</sup> <sub>-0.007</sub>
G <sub>Fe</sub>	Energy (keV)	6.64 <sup>+0.03</sup> <sub>-0.04</sub>	6.54 <sup>+0.05</sup> <sub>-0.05</sub>	> 6.83	6.75 <sup>+0.09</sup> <sub>-0.11</sub>	-
	$\sigma$ (keV)	< 0.11	< 0.17	0.03 <sup>*1</sup>	0.001 <sup>*1</sup>	-
	normalization ( $10^{-5}$ photons $\text{s}^{-1} \text{cm}^{-2}$ )	0.47 <sup>+0.19</sup> <sub>-0.19</sub>	0.42 <sup>+0.18</sup> <sub>-0.18</sub>	0.37 <sup>+0.32</sup> <sub>-0.32</sub>	0.80 <sup>+0.41</sup> <sub>-0.41</sub>	-
const <sub>cross</sub>	FPMA/XMM-pn	-	-	-	1.28 <sup>+0.02</sup> <sub>-0.02</sub>	-
	FPMB/XMM-pn	-	-	-	1.24 <sup>+0.02</sup> <sub>-0.02</sub>	-
	FPMA/Swift-XRT	-	-	-	-	1.25 <sup>+0.03</sup> <sub>-0.04</sub>
	FPMB/Swift-XRT	-	-	-	-	1.21 <sup>+0.01</sup> <sub>-0.01</sub>
$\chi^2/\text{d.o.f}$		1.14	1.13	1.01	1.01	1.54

\*1 not constrained

large as  $\Omega/2\pi \approx 0.8$ , that is much greater than the observed value. Thus, it is more likely that the inner edge of the disk does *not* reach the ISCO ( $6 R_g$ ), but is rather *truncated* at around a few tens of  $R_g$ . If the X-ray corona size is  $\sim 10 R_g$ , the innermost radius of the disk is  $\approx 30 R_g$  to give the observed value  $\Omega/2\pi \approx 0.3$ .

In the spectral fitting with the `relxill` model, we fixed the inner disk radius ( $r_{\text{in}} = 6 R_g$ ) and the black hole spin ( $a = 0$ ) assuming a Schwarzschild black hole. Even when we changed the inner disk radius in the range of  $6 R_g \leq r_{\text{in}} \leq 50 R_g$  with  $a = 0$  and all the other parameters fixed, the spectral fitting did not show significant changes. Similarly, even when we changed the black hole spin ( $0 \leq a < 1$ ) with the disk inner radius fixed to the ISCO, the spectral fitting result hardly changes. Therefore, we can hardly constrain the inner disk radius and the black hole spin in our model.

## 4.2 Geometry of partial covering clouds and UFOs

The schematic picture of the clumps in the wind is shown in Fig. 6. For the geometry of the partial covering clouds, Risaliti et al. (2011a) proposed that the absorber in Mrk 766 has a cometary-like structure with a neutral core and an ionized tail. Also, the double-

layer absorber with internal structure has been proposed in other AGNs (e.g., Miyakawa et al. 2012; Iso et al. 2016). Another scenario suggests that the cold clumps are embedded in the ionized wind and are subjected to the X-ray illumination and a pressure balance (Done & Jin 2016; Elvis 2000). This will invoke a thermal instability in the ionized gas and the emergence of cooler clumps (Krolik et al. 1981). Furthermore, recent numerical hydrodynamic simulations predict the emergence of clumpy outflows (e.g., Takeuchi et al. 2013; Kobayashi et al. 2018), so that the ‘‘hot-inner and clumpy-outer winds’’ model successfully explains spectral variations of several bright Seyfert galaxies (Mizumoto et al. 2019a; Midooka et al. 2022).

Regardless of minor differences in the models and interpretations, it is generally accepted that there are fast and hot flows near the black hole (i.e., UFO), and the partial covering clouds farther from the black hole. We find that the partial covering fraction of the partial covering clouds is lower when the UFOs velocity gets higher (Fig. 7). This relation is exactly consistent with the results of hydrodynamic simulations that the covering fraction and the UFO velocity anti-correlate as long as the mass outflow rate and the clump formation radius are invariable (see, e.g., Eq. 19 in Takeuchi et al. 2013). We note that this correlation is statistically significant at the 90 %

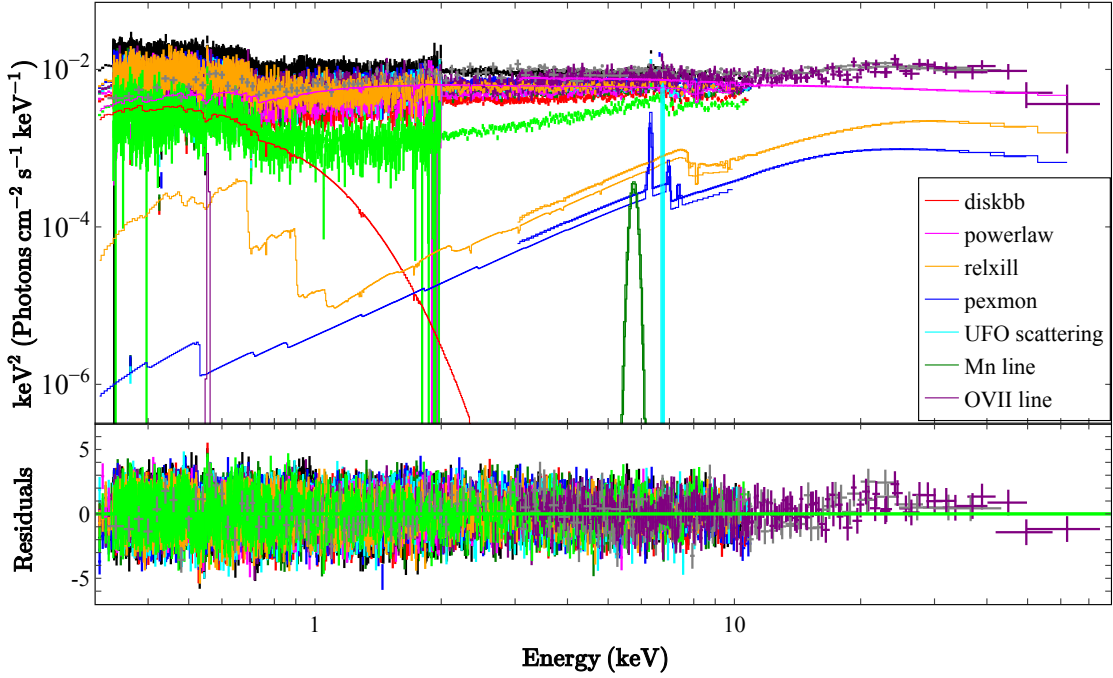


**Figure 3.** Result of the simultaneous spectra fitting of the 10 datasets with the double partial covering model in 0.3 – 79 keV. Data points and residuals of the 10 datasets, XMM1–8, XMM9&Nu11 and Nu10&Sw12 are represented with different colors as follows; orange (XMM1), black (XMM2), green (XMM3), red (XMM4), green (XMM5), blue (XMM6), cyan (XMM7), magenta (XMM8), purple (XMM9 & Nu11), and gray (Nu10 & Sw12). Individual spectral model components (from diskbb to O VII line) to fit XMM9 & Nu11 are shown in different colors.

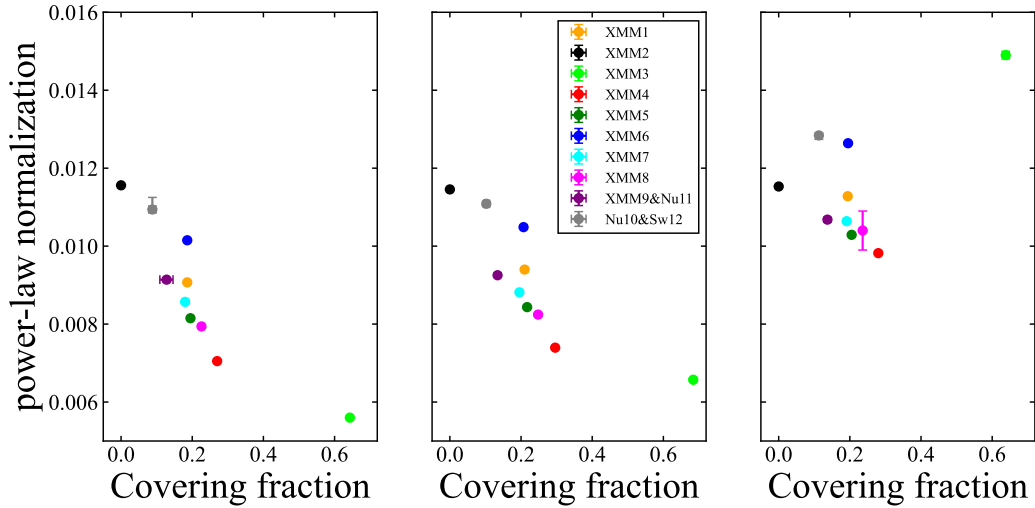


**Figure 4.** Relation between the partial covering fraction and the power-law normalization. The left panel is the result of the double partial covering model, the center panel is the result of adding the *cabs* model, and the right panel is the result of the triple partial covering model. The datasets are distinguished by different colors.

confidence level but not 95 %, with the Pearson coefficient of  $-0.61$  and the p-value of 0.08. It will be important to determine more accurately the UFO velocities and partial covering fractions in future microcalorimeter observations.

The UFO location is estimated as follows; the minimum radius is estimated by the balancing equation between gravitational potential and kinetic energy, as

$$r_{\min} = \frac{2GM_{\text{BH}}}{v_{\text{out}}^2}, \quad (3)$$

and the maximum radius is estimated from the definition of the ionization parameter under the condition that  $nr \sim N_{\text{H}}$  and  $L$  is the X-ray luminosity in 13.6 eV–13.6 keV, as

$$r_{\max} = \frac{L}{\xi N_{\text{H}}}. \quad (4)$$

The average parameters of UFOs in this study are  $N_{\text{H}} \sim 2.1 \times 10^{23} \text{cm}^{-2}$ ,  $\log \xi \sim 4.2$  and velocity  $\sim -0.10c$ . Then, the UFO is considered to locate in the range of  $\sim 10^2 R_g - 10^3 R_g$ .

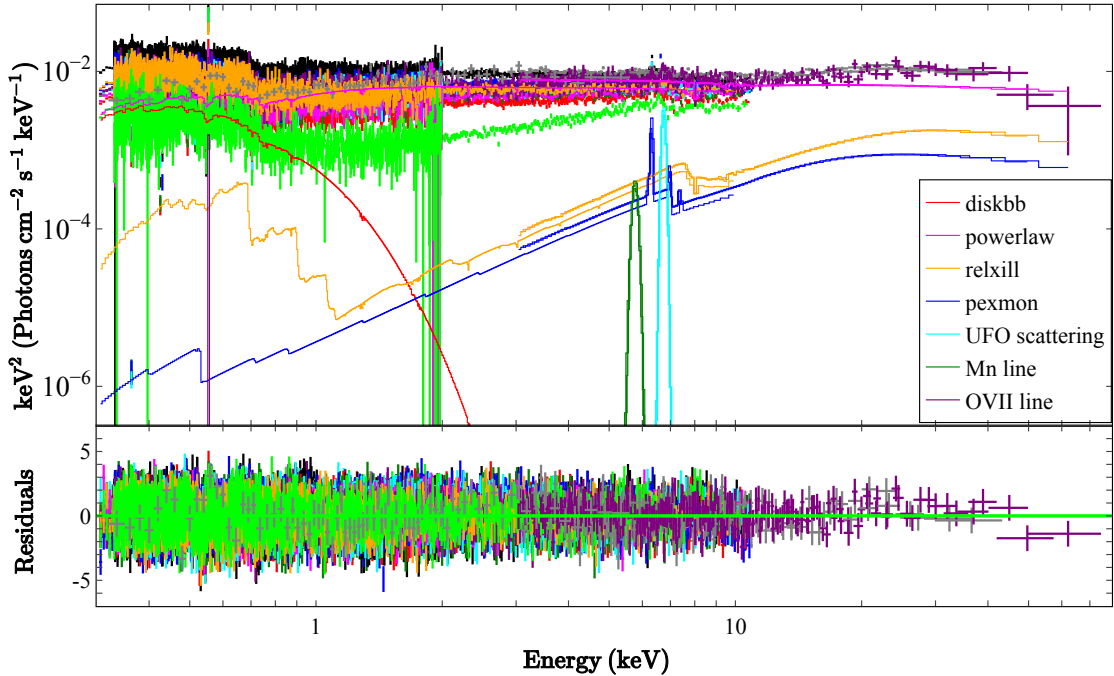


**Figure 5.** Result of the simultaneous spectra fitting of the 10 datasets with the triple partial covering model in 0.3-79 keV. See the caption of Fig. 3 for other explanation.

**Table 6.** Fitting results of the tied parameters with the triple-layer partial covering model.

model	parameter	value
zTBabs	$N_{\text{H}} (10^{20} \text{cm}^{-2})$	$1.67^{+0.02}_{-0.00}$
$W_1$	$N_{\text{H}} (10^{23} \text{cm}^{-2})$	$3.89^{+0.08}_{-0.08}$
	$\log \xi$	$1.70^{+0.01}_{-0.01}$
$W_2$	$N_{\text{H}} (10^{22} \text{cm}^{-2})$	$1.79^{+0.03}_{-0.02}$
	$\log \xi$	$< -2$
$W_3$	$N_{\text{H}} (10^{21} \text{cm}^{-2})$	$2.79^{+0.01}_{-0.02}$
	$\log \xi$	$0.474^{+0.004}_{-0.004}$
$W_5$	$N_{\text{H}} (10^{24} \text{cm}^{-2})$	$4.9^{+1.5}_{-0.9}$
diskbb	$T_{\text{in}} (\text{keV})$	$0.1291^{+0.0001}_{-0.0001}$
powerlaw	$\Gamma$	$2.210^{+0.001}_{-0.001}$
relxill	$\log \xi$	$0.49^{+0.02}_{-0.04}$
const <sub>ref</sub>	powerlaw ratio	$0.0063^{+0.0002}_{-0.0003}$
pexmon	Reflection rate	$-0.20^{+0.01}_{-0.01}$
$G_{\text{OVII}}$	Energy (keV)	$0.5543^{+0.0001}_{-0.0004}$
	$\sigma$ (keV)	$< 0.0004$
	normalization ( $10^{-5} \text{photons s}^{-1} \text{cm}^{-2}$ )	$2.8^{+0.6}_{-0.3}$
$G_{\text{Mn}}$	Energy (keV)	$5.76^{+0.05}_{-0.07}$
	$\sigma$ (keV)	$0.07^{*1}$
const <sub>Mn</sub>	powerlaw ratio	$0.0002^{+0.0001}_{-0.0001}$

\*1 not constrain

### 4.3 Spectral variability

The right panel of Fig. 4 depicts the power-law normalization and the partial covering fraction in the triple partial covering model. The power-law normalization exhibits a change of a factor of  $\sim 1.5$  while the covering fraction changes by a factor of  $\sim 5$ . This implies that while the hard X-ray variation ( $\geq 10$  keV) is due to the power-law normalization changes, the soft X-rays ( $\leq 10$  keV) are more significantly affected by the partial covering fraction. We have explained the spectral variability over the  $\sim 15$  years assuming no changes of the power-law photon index, the column densities and ionization parameters of the triple-layered partial absorbers ( $W_1$ ,  $W_2$  and  $W_5$ ) and the warm absorber ( $W_3$ ).

Our spectral datasets consist of the 10 observations, each of which has  $\sim$ day exposure, over  $\sim 15$  years (Table 1). All the UFO parameters ( $W_4$ ), namely the column density, ionization state and velocity, are variable for different spectra, as well as the partial covering fraction. Risaliti et al. (2011b) examined timescales of the partial covering change from the flux and hardness-ratio variations. They estimated that the location of the partial covering clouds is at  $\sim 10^3 R_g - 10^4 R_g$ . We naturally think that the partial covering clouds are outer UFO with respect to these locations. Considering that the corona (a few tens of  $R_g$ ) is partially covered by the partial covering clouds, we estimate the size of the partial covering clouds  $\lesssim 10^{13}$  cm.

These differences in the variation timescales of the different absorbers reflect locations of the multiple absorbers around the black hole, and are consistent with the ‘‘hot-inner and clumpy-outer wind scenario’’ (Fig. 6; Mizumoto et al. 2019a). The hot-inner outflow (UFO) is produced at the inner-part of the accretion disk, which turns into the clumpy-outer wind (partial covering clouds, a.k.a. ‘‘obscurers’’; Kaastra et al. 2014). The warm absorber may be produced by irradiation and evaporation of the outer torus (Mizumoto et al. 2019b).



**Table 7.** Fitting results of the free parameters with the triple-layer partial covering model

model	parameter	XMM1	XMM2	XMM3	XMM4	XMM5
W <sub>1</sub> &W <sub>2</sub> &W <sub>5</sub>	$\alpha$	0.194 <sup>+0.001</sup> <sub>-0.001</sub>	< 0.000	0.638 <sup>+0.001</sup> <sub>-0.000</sub>	0.280 <sup>+0.001</sup> <sub>-0.001</sub>	0.205 <sup>+0.001</sup> <sub>-0.001</sub>
W <sub>4</sub>	$N_{\text{H}}$ ( $10^{23}$ cm <sup>-2</sup> )	0.70 <sup>+0.18</sup> <sub>-0.13</sub>	< 0.99	0.83 <sup>+0.17</sup> <sub>-0.19</sub>	1.08 <sup>+0.49</sup> <sub>-0.48</sub>	2.8 <sup>+1.5</sup> <sub>-1.2</sub>
	log $\xi$	3.71 <sup>+0.06</sup> <sub>-0.05</sub>	5.0* <sup>1</sup>	3.68 <sup>+0.18</sup> <sub>-0.15</sub>	3.96 <sup>+0.12</sup> <sub>-0.10</sub>	4.29 <sup>+0.21</sup> <sub>-0.14</sub>
	vturb ( $10^3$ km s <sup>-1</sup> )	1.2 <sup>+0.6</sup> <sub>-0.5</sub>	0.1* <sup>1</sup>	5.3 <sup>+3.3</sup> <sub>-3.5</sub>	< 0.62	< 0.19
	z	-0.101 <sup>+0.002</sup> <sub>-0.002</sub>	-0.271(fixed)	-0.038 <sup>+0.003</sup> <sub>-0.003</sub>	-0.065 <sup>+0.001</sup> <sub>-0.002</sub>	-0.066 <sup>+0.003</sup> <sub>-0.002</sub>
diskbb	normalization ( $10^3$ )	11.28 <sup>+0.07</sup> <sub>-0.09</sub>	8.87 <sup>+0.03</sup> <sub>-0.03</sub>	55.0 <sup>+0.3</sup> <sub>-0.3</sub>	9.57 <sup>+0.05</sup> <sub>-0.06</sub>	8.64 <sup>+0.04</sup> <sub>-0.05</sub>
powerlaw	normalization ( $10^{-2}$ photons s <sup>-1</sup> cm <sup>-2</sup> keV <sup>-1</sup> )	1.128 <sup>+0.004</sup> <sub>-0.004</sub>	1.153 <sup>+0.003</sup> <sub>-0.001</sub>	1.49 <sup>+0.01</sup> <sub>-0.01</sub>	0.982 <sup>+0.003</sup> <sub>-0.003</sub>	1.029 <sup>+0.002</sup> <sub>-0.003</sub>
G <sub>Fe</sub>	Energy (keV)	6.60 <sup>+0.14</sup> <sub>-0.14</sub>	< 6.53	6.56 <sup>+0.05</sup> <sub>-0.05</sub>	6.41 <sup>+0.07</sup> <sub>-0.07</sub>	6.66 <sup>+0.09</sup> <sub>-0.10</sub>
	$\sigma$ (keV)	0.19 <sup>+0.15</sup> <sub>-0.09</sub>	0.42 <sup>+0.08</sup> <sub>-0.06</sub>	< 0.13	0.13 <sup>+0.07</sup> <sub>-0.05</sub>	0.19 <sup>+0.09</sup> <sub>-0.07</sub>
	normalization ( $10^{-5}$ photons s <sup>-1</sup> cm <sup>-2</sup> )	0.98 <sup>+0.45</sup> <sub>-0.45</sub>	3.97 <sup>+0.41</sup> <sub>-0.41</sub>	0.52 <sup>+0.17</sup> <sub>-0.16</sub>	0.71 <sup>+0.22</sup> <sub>-0.22</sub>	0.81 <sup>+0.26</sup> <sub>-0.26</sub>
$\chi^2/\text{d.o.f}$		1.13	1.32	1.34	1.13	1.17
model	parameter	XMM6	XMM7	XMM8	XMM9&Nu11	Nu10&Sw12
W <sub>1</sub> &W <sub>2</sub> &W <sub>5</sub>	$\alpha$	0.195 <sup>+0.001</sup> <sub>-0.001</sub>	0.191 <sup>+0.001</sup> <sub>-0.001</sub>	0.237 <sup>+0.001</sup> <sub>-0.001</sub>	0.137 <sup>+0.002</sup> <sub>-0.002</sub>	0.113 <sup>+0.004</sup> <sub>-0.003</sub>
W <sub>4</sub>	$N_{\text{H}}$ ( $10^{23}$ cm <sup>-2</sup> )	1.63 <sup>+0.87</sup> <sub>-0.61</sub>	1.02 <sup>+0.60</sup> <sub>-0.38</sub>	0.36 <sup>+0.55</sup> <sub>-0.14</sub>	> 5.3	> 6.9
	log $\xi$	4.45 <sup>+0.20</sup> <sub>-0.15</sub>	4.13 <sup>+0.17</sup> <sub>-0.13</sub>	3.77 <sup>+0.21</sup> <sub>-0.10</sub>	> 4.59	4.40 <sup>+0.10</sup> <sub>-0.11</sub>
	vturb ( $10^3$ km s <sup>-1</sup> )	0.3 <sup>+1.4</sup> <sub>-0.2</sub>	> 7.2	< 6.2	< 0.98	< 0.18
	z	-0.068 <sup>+0.002</sup> <sub>-0.001</sub>	-0.052 <sup>+0.002</sup> <sub>-0.001</sub>	-0.066 <sup>+0.002</sup> <sub>-0.003</sub>	-0.146 <sup>+0.020</sup> <sub>-0.002</sub>	-0.088 <sup>+0.013</sup> <sub>-0.011</sub>
diskbb	normalization ( $10^3$ )	10.07 <sup>+0.04</sup> <sub>-0.06</sub>	7.70 <sup>+0.04</sup> <sub>-0.05</sub>	8.05 <sup>+0.08</sup> <sub>-0.10</sub>	6.20 <sup>+0.11</sup> <sub>-0.12</sub>	< 0.49
powerlaw	normalization ( $10^{-2}$ photons s <sup>-1</sup> cm <sup>-2</sup> keV <sup>-1</sup> )	1.264 <sup>+0.003</sup> <sub>-0.003</sub>	1.064 <sup>+0.002</sup> <sub>-0.003</sub>	1.04 <sup>+0.05</sup> <sub>-0.05</sub>	1.068 <sup>+0.006</sup> <sub>-0.006</sub>	1.284 <sup>+0.007</sup> <sub>-0.010</sub>
G <sub>Fe</sub>	Energy (keV)	6.64 <sup>+0.03</sup> <sub>-0.04</sub>	6.56 <sup>+0.08</sup> <sub>-0.08</sub>	> 6.82	6.75 <sup>+0.10</sup> <sub>-0.09</sub>	-
	$\sigma$ (keV)	< 0.14	< 0.21	< 0.48	0.001* <sup>1</sup>	-
	normalization ( $10^{-5}$ photons s <sup>-1</sup> cm <sup>-2</sup> )	0.53 <sup>+0.19</sup> <sub>-0.19</sub>	0.58 <sup>+0.23</sup> <sub>-0.23</sub>	0.41 <sup>+0.33</sup> <sub>-0.35</sub>	0.98 <sup>+0.43</sup> <sub>-0.43</sub>	-
const <sub>cross</sub>	FPMA/XMM-pn	-	-	-	1.28(fixed)	-
	FPMB/XMM-pn	-	-	-	1.24(fixed)	-
	FPMA/Swift-XRT	-	-	-	-	1.25(fixed)
	FPMB/Swift-XRT	-	-	-	-	1.21(fixed)
$\chi^2/\text{d.o.f}$		1.13	1.13	1.01	1.00	1.47

\*1 not constrained

#### 4.4 Scattering in the ionized absorber

We have introduced a positive Gaussian at 6.4–6.7 keV as G<sub>Fe</sub> (§3.3; Fig. 2). Importance of the scattering by surrounding material in Mrk 766 has already been pointed out (e.g., Miller et al. 2006; Turner et al. 2007; Sim et al. 2008), so that the origin of the Gaussian line is likely the Fe-K resonance scattering produced by the ionized material out of the line-of-sight. The average peak energy of the emission line is ~6.61 keV, which is consistent with the ionization state of the UFO (log  $\xi$  ~ 4.2) (e.g., Kallman & Bautista 2001; Kallman et al. 2004), supporting the idea that this line results from the resonance scattering in the UFO. In fact, Mizumoto et al. (2021) suggested that the UFO material out of the line-of-sight should induce resonance scattering line (shown with the cyan line in Fig. 6). Via X-ray spectral synthesis with a radiation hydrodynamic simulation, Mizumoto et al. (2021) demonstrated that the equivalent width (EW) of the Fe-K resonance emission lines ranges from ~0.02 – 0.05 keV and remains relatively constant with respect to the viewing angle, while that of the UFO’s absorption lines experiences a significant change from –0.18 keV to null as the viewing angle changes (see also, e.g., Hagino et al. 2015). The observed EWs of the G<sub>Fe</sub> and the UFO’s absorption line (Table

**Table 8.** The emission/absorption equivalent width of Fe-K with the triple partial covering model.

Data	Emission EW (keV)	Absorption EW (keV)* <sup>1</sup>
XMM1	0.063 <sup>+0.029</sup> <sub>-0.029</sub>	-0.134
XMM2	0.187 <sup>+0.019</sup> <sub>-0.019</sub>	-0.001
XMM3	0.056 <sup>+0.018</sup> <sub>-0.017</sub>	-0.164
XMM4	0.056 <sup>+0.017</sup> <sub>-0.017</sub>	-0.122
XMM5	0.061 <sup>+0.032</sup> <sub>-0.032</sub>	-0.073
XMM6	0.031 <sup>+0.011</sup> <sub>-0.011</sub>	-0.068
XMM7	0.039 <sup>+0.015</sup> <sub>-0.015</sub>	-0.092
XMM8	0.037 <sup>+0.030</sup> <sub>-0.032</sub>	-0.063
XMM9 & Nu11	0.067 <sup>+0.029</sup> <sub>-0.029</sub>	-0.108
Nu10 & Sw12	0	-0.216
Average	0.052	-0.104

\*1 Errors are less than 1%.

8) are consistent with the simulation when the UFO is observed at an inclination angle of 45° – 55°.

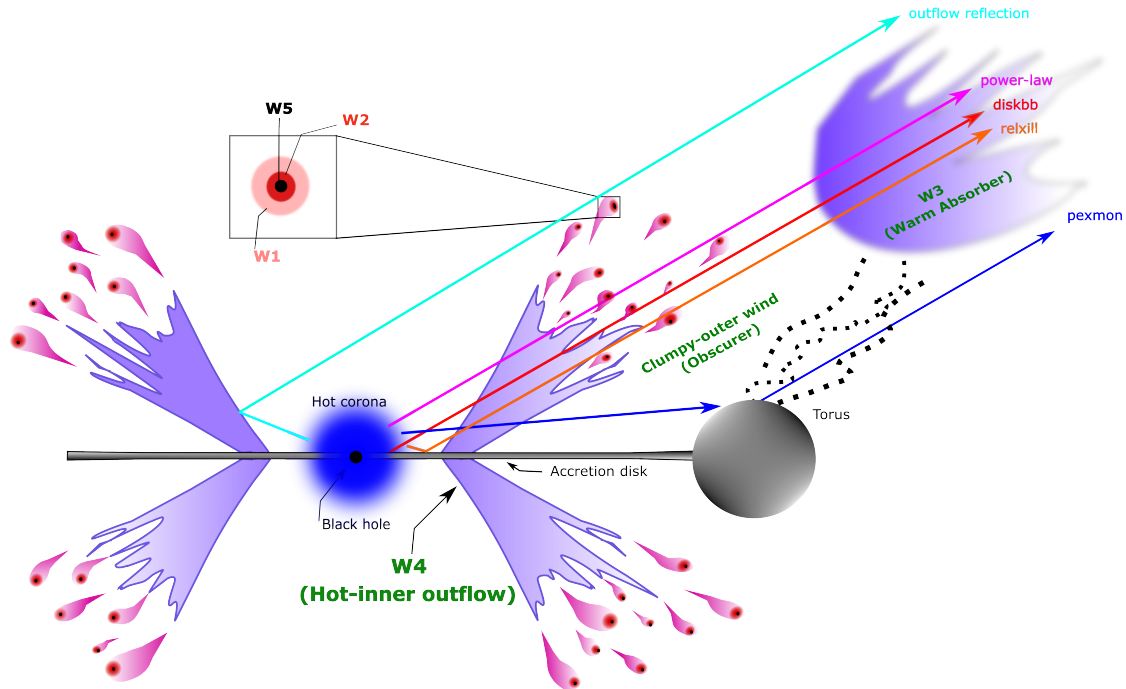


**Figure 6.** Assumed geometry of Mrk 766. Arrows with different colors represent different X-ray emission components. There are three distinct intervening absorbers; the clumpy-outer winds with internal layers ( $W_1$ ,  $W_2$ , and  $W_5$ ), the hot-inner outflow corresponding to the UFO ( $W_4$ ), and the warm absorber ( $W_3$ ). The original figure made for NGC5548 by Midooka et al. (2022) was modified considering the differences between the two sources.

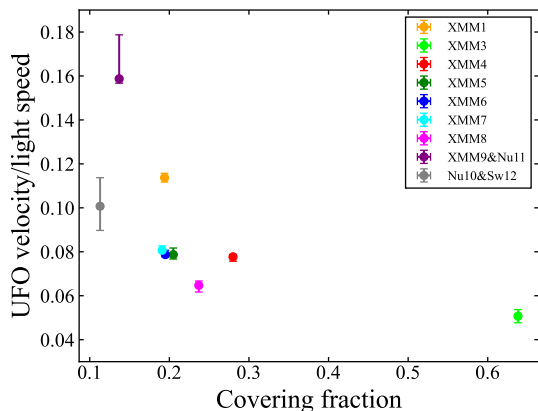


**Figure 7.** Relation between the partial covering fractions (with the triple partial covering model) and the UFO velocities. XMM2 data are not used where the UFO feature was not clear.

## 5 CONCLUSION

In this paper, we tried to solve the origins of the complex iron K-line structure and the significant X-ray spectral variations in 0.3 – 79 keV of Mrk 766 with a simple model. We used 10 spectral datasets taken over ~15 years from 2000 to 2015; nine observation sequences of *XMM-Newton*, one of which was simultaneous with *NuSTAR*, and another observation of *NuSTAR* which was simultaneous with *Swift*. The energy spectra are largely explained by a simple geometry that a moderately extended central X-ray region emitting a power-law spectrum is affected by several distinct absorption zones in the line-of-sight; the hot and fast inner outflow (UFO), the outer-clumpy

winds (partial covering clouds) comprising multiple ionization layers, and the warm absorber further outward. Spectral variations are mainly explained due to changes in the partial covering fraction, the power-law normalization, and the UFO parameters. Other spectral parameters are not significantly variable over ~15 years.

Additionally, a slightly broadened Fe-K emission line is required at ~6.4–6.7keV with the intrinsic width ( $1\sigma$ ) 0.1–0.3 keV and the equivalent width ~0.05 keV. This emission line is considered to be produced by the X-ray scattering in the UFO out of the line-of-sight.

## ACKNOWLEDGEMENTS

We thank the anonymous referee for valuable comments and suggestions to improve this paper. This research has made use of data and/or software provided by the High Energy Astrophysics Science Archive Research Center (HEASARC), which is a service of the Astrophysics Science Division at NASA/GSFC. We used data by *XMM-Newton* led by the European Space Agency’s (ESA). This study also used data of *NuSTAR* led by the California Institute of Technology (Caltech) and managed by NASA’s Jet Propulsion Laboratory in Pasadena, and of *Swift* which is based on the Mission Operations Center (MOC) operated by the Pennsylvania State University and NASA. The authors used JAXA Supercomputer System generation 3 (JSS3). This research was supported by JSPS KAKENHI Grant Number JP21K13958 (MM). MM acknowledges support from the Hakubi project at Kyoto University. The authors thank Prof. Kyoko Matsushita and Dr. Shogo B. Kobayashi for discussion. The authors thank Ms. Juriko Ebisawa for the artwork (Fig. 6).

## DATA AVAILABILITY

All the observational data used in this paper are publicly available. They can be accessed via HEASARC Browse:  
<https://heasarc.gsfc.nasa.gov/db-perl/W3Browse/w3browse.pl>

## ORCID IDS

Yuto Mochizuki   
<https://orcid.org/0000-0003-3224-1821>  
 Misaki Mizumoto   
<https://orcid.org/0000-0003-2161-0361>  
 Ken Ebisawa   
<https://orcid.org/0000-0002-5352-7178>

## REFERENCES

- Adelman-McCarthy J. K., et al., 2011, *VizieR Online Data Catalog*, p. II/306  
 Arnaud K. A., 1996, in Jacoby G. H., Barnes J., eds, *Astronomical Society of the Pacific Conference Series Vol. 101, Astronomical Data Analysis Software and Systems V*. p. 17  
 Bentz M. C., Katz S., 2015, *PASP*, **127**, 67  
 Buisson D. J. K., et al., 2018, *MNRAS*, **480**, 3689  
 Danehkar A., Nowak M. A., Lee J. C., Smith R. K., 2018, *PASP*, **130**, 024501  
 Dauser T., Garcia J., Parker M. L., Fabian A. C., Wilms J., 2014, *MNRAS*, **444**, L100  
 Dauser T., García J. A., Joyce A., Licklederer S., Connors R. M. T., Ingram A., Reynolds C. S., Wilms J., 2022, *MNRAS*, **514**, 3965  
 Done C., Jin C., 2016, *MNRAS*, **460**, 1716  
 Elvis M., 2000, *ApJ*, **545**, 63  
 Fabian A. C., Rees M. J., Stella L., White N. E., 1989, *MNRAS*, **238**, 729  
 Fabian A. C., et al., 2009, *Nature*, **459**, 540  
 Gabriel C., et al., 2004, in Oehsenbein F., Allen M. G., Egret D., eds, *Astronomical Society of the Pacific Conference Series Vol. 314, Astronomical Data Analysis Software and Systems (ADASS) XIII*. p. 759  
 García J., et al., 2014, *ApJ*, **782**, 76  
 Gardner E., Done C., 2015, *MNRAS*, **448**, 2245  
 Gehrels N., et al., 2004, *ApJ*, **611**, 1005  
 Grevesse N., Sauval A. J., 1998, *Space Sci. Rev.*, **85**, 161  
 Hagino K., Odaka H., Done C., Gandhi P., Watanabe S., Sako M., Takahashi T., 2015, *MNRAS*, **446**, 663  
 Harrison F. A., et al., 2013, *ApJ*, **770**, 103  
 Iso N., Ebisawa K., Sameshima H., Mizumoto M., Miyakawa T., Inoue H., Yamasaki H., 2016, *PASJ*, **68**, S27  
 Jansen F., et al., 2001, *A&A*, **365**, L1  
 Kaastra J. S., et al., 2014, *Science*, **345**, 64  
 Kalberla P. M. W., Burton W. B., Hartmann D., Arnal E. M., Bajaja E., Morras R., Pöppel W. G. L., 2005, *A&A*, **440**, 775  
 Kallman T., Bautista M., 2001, *ApJS*, **133**, 221  
 Kallman T. R., Palmeri P., Bautista M. A., Mendoza C., Krolik J. H., 2004, *ApJS*, **155**, 675  
 Kobayashi H., Ohsuga K., Takahashi H. R., Kawashima T., Asahina Y., Takeuchi S., Mineshige S., 2018, *PASJ*, **70**, 22  
 Krolik J. H., McKee C. F., Tarter C. B., 1981, *ApJ*, **249**, 422  
 Liebmann A. C., Haba Y., Kunieda H., Tsuruta S., Takahashi M., Takahashi R., 2014, *ApJ*, **780**, 35  
 Magdziarz P., Zdziarski A. A., 1995, *MNRAS*, **273**, 837  
 Maiolino R., et al., 2010, *A&A*, **517**, A47  
 Makishima K., Maejima Y., Mitsuda K., Bradt H. V., Remillard R. A., Tuohy I. R., Hoshi R., Nakagawa M., 1986, *ApJ*, **308**, 635  
 Midooka T., Ebisawa K., Mizumoto M., Sugawara Y., 2022, *MNRAS*, **513**, 5020  
 Miller L., Turner T. J., Reeves J. N., George I. M., Porquet D., Nandra K., Dovciak M., 2006, *A&A*, **453**, L13  
 Miller L., Turner T. J., Reeves J. N., George I. M., Kraemer S. B., Wingert B., 2007, *A&A*, **463**, 131  
 Mitsuda K., et al., 1984, *PASJ*, **36**, 741  
 Miyakawa T., Ebisawa K., Inoue H., 2012, *PASJ*, **64**, 140  
 Mizumoto M., Ebisawa K., Sameshima H., 2014, *PASJ*, **66**, 122  
 Mizumoto M., Ebisawa K., Tsujimoto M., Done C., Hagino K., Odaka H., 2019a, *Monthly Notices of the Royal Astronomical Society*, **482**, 5316  
 Mizumoto M., Done C., Tomaru R., Edwards I., 2019b, *MNRAS*, **489**, 1152  
 Mizumoto M., Nomura M., Done C., Ohsuga K., Odaka H., 2021, *MNRAS*, **503**, 1442  
 Nandra K., O'Neill P. M., George I. M., Reeves J. N., 2007, *MNRAS*, **382**, 194  
 Ogawa S., Ueda Y., Yamada S., Tanimoto A., Kawaguchi T., 2019, *ApJ*, **875**, 115  
 Pounds K. A., Reeves J. N., Page K. L., Wynn G. A., O'Brien P. T., 2003a, *MNRAS*, **342**, 1147  
 Pounds K. A., Reeves J. N., King A. R., Page K. L., O'Brien P. T., Turner M. J. L., 2003b, *MNRAS*, **345**, 705  
 Reeves J. N., et al., 2009, *ApJ*, **701**, 493  
 Risaliti G., et al., 2009a, *MNRAS*, **393**, L1  
 Risaliti G., et al., 2009b, *ApJ*, **696**, 160  
 Risaliti G., Nardini E., Salvati M., Elvis M., Fabbiano G., Maiolino R., Pietrini P., Torricelli-Ciamponi G., 2011a, *MNRAS*, **410**, 1027  
 Risaliti G., Nardini E., Elvis M., Brenneman L., Salvati M., 2011b, *MNRAS*, **417**, 178  
 Sim S. A., Long K. S., Miller L., Turner T. J., 2008, *MNRAS*, **388**, 611  
 Strüder L., et al., 2001, *A&A*, **365**, L18  
 Takeuchi S., Ohsuga K., Mineshige S., 2013, *PASJ*, **65**, 88  
 Tanimoto A., Ueda Y., Odaka H., Kawaguchi T., Fukazawa Y., Kawamuro T., 2019, *ApJ*, **877**, 95  
 Tombesi F., Cappi M., Reeves J. N., Palumbo G. G. C., Braito V., Dadina M., 2011, *ApJ*, **742**, 44  
 Tombesi F., Cappi M., Reeves J. N., Nemmen R. S., Braito V., Gaspari M., Reynolds C. S., 2013, *MNRAS*, **430**, 1102  
 Turner T. J., Miller L., Reeves J. N., Kraemer S. B., 2007, *A&A*, **475**, 121  
 Verner D. A., Ferland G. J., Korista K. T., Yakovlev D. G., 1996, *ApJ*, **465**, 487  
 Wilms J., Allen A., McCray R., 2000, *ApJ*, **542**, 914  
 Yamasaki H., Mizumoto M., Ebisawa K., Sameshima H., 2016, *PASJ*, **68**, 80  
 den Herder J. W., et al., 2001, *A&A*, **365**, L7

This paper has been typeset from a  $\text{\TeX}/\text{\LaTeX}$  file prepared by the author.